STRUCTURAL CHEMISTRY

ISSN 2053-2296

The cleavage of indinavir sulfate: synthesis and characterization of a *cis*-1-amino-2-indanol salt

Tebogo M. L. Mokoto,[a,b] Andreas Lemmerer,[c] Yasien Sayed,[a] Kgaugelo C. Tapala,[b] Itumeleng B. Setshedi[d] and Mark G. Smith[b]*

[a]Protein Structure-Function Research Unit, School of Molecular and Cell Biology, University of the Witwatersrand, Johannesburg, Gauteng, South Africa, [b]University of South Africa, Department of Chemistry, Unisa Science Campus, Roodepoort, Gauteng, South Africa, [c]Molecular Sciences Institute, School of Chemistry, University of the Witwatersrand, Johannesburg, Gauteng, South Africa, and [d]University of South Africa, Department of Life and Consumer Sciences, Unisa Science Campus, Roodepoort, Gauteng, South Africa. *Correspondence e-mail: smithm2@unisa.ac.za

Received 5 May 2025
Accepted 26 June 2025

Edited by R. Diniz, Universidade Federal de Minas Gerais, Brazil

Keywords: crystal structure; indinavir; solvation crystallization; salt crystal structure; slow evaporation; thermal analysis; surface analysis; chemical transformations.

CCDC reference: 2324379

Supporting information: this article has supporting information at journals.iucr.org/c

The HIV-1 protease inhibitor indinavir sulfate was cleaved *via* a one-pot reflux synthesis using 1-propanol, yielding the salt bis(2-hydroxy-2,3-dihydro-1*H*-inden-1-aminium) sulfate, $2C_9H_{12}NO^+\cdot SO_4^{2-}$. Single-crystal X-ray diffraction (SC-XRD) revealed that the salt crystallizes in the monoclinic space group $P2_1$. The structure consists of two conformationally distinct cations and one sulfate anion, stabilized through an extensive hydrogen-bonding network. Thermal analysis showed minor solvent loss around 200 °C, followed by a two-step decomposition process commencing at 306.6 °C. Hirshfeld surface analysis revealed dominant O···H/H···O (44.4–41.0%) and H···H (45.2–40.1%) intermolecular contacts, with minor contributions from C···H/H···C and C···O/O···C interactions. These contact percentages were calculated for each of the two independent cations. The van der Waals surface area (687.30 Å^2) accounts for 71.43% of the unit cell. These results provide structural and thermal evidence for the transformation of indinavir sulfate under alcoholytic conditions, highlighting the formation and stabilization of the resulting salt.

1. Introduction

Amino alcohols are primarily derived from a diverse range of chiral compounds, offering significant advantages due to their conformational properties and structural diversity in drug design (Matamoros *et al.*, 2023). One notable compound in this category is *cis*-1-amino-2-indanol, a versatile building block in pharmaceutical formulations. Its applications extend to the synthesis of antimalarial drugs and HIV-1 protease inhibitors, where it plays a critical role. This compound is frequently used as a rigid scaffold for covalently attached chiral auxiliary molecules, acts as a resolving agent for secondary alcohols and can function as a racemic carboxylic acid. Furthermore, it is instrumental in the catalytic enantioselective synthesis of various molecules (Gallou & Senanayake, 2006). Among amino alcohols, *cis*-1-amino-2-indanol is of considerable pharmaceutical significance (Gallou & Senanayake, 2006). It was first introduced as a chiral amino alcohol P2′ ligand in the development of HIV protease inhibitors, culminating in Merck's discovery of the potent inhibitor L-685,434, commonly known as indinavir (Dorsey *et al.*, 1994). This chiral compound has been recognised as a pivotal ligand in the development of HIV-PR inhibitors, with various strategies employed to synthesize different asymmetric constrained phenyl glycinol surrogates. Its sterically bulky indane structure, combined with the restricted *cis*-aminoindanol moiety, constrains the formation of an effective chiral discriminative

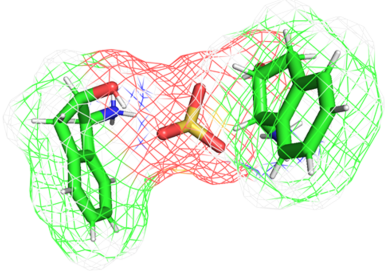

Table 1
Experimental details.

Crystal data	
Chemical formula	$2C_9H_{12}NO^+\cdot SO_4^{2-}$
M_r	396.47
Crystal system, space group	Monoclinic, $P2_1$
Temperature (K)	123
a, b, c (Å)	11.6412 (10), 6.4226 (4), 12.8761 (10)
β (°)	103.791 (4)
V (Å^3)	934.95 (12)
Z	2
Radiation type	Mo $K\alpha$
μ (mm^{-1})	0.21
Crystal size (mm)	0.57 × 0.11 × 0.03
Data collection	
Diffractometer	Bruker APEXII CCD
No. of measured, independent and observed [$I \geq 2\sigma(I)$] reflections	26758, 3458, 2956
R_{int}	0.098
$(\sin \theta/\lambda)_{max}$ (Å^{-1})	0.606
Refinement	
$R[F^2 > 2\sigma(F^2)]$, $wR(F^2)$, S	0.045, 0.111, 1.04
No. of reflections	3454
No. of parameters	276
No. of restraints	1
H-atom treatment	H atoms treated by a mixture of independent and constrained refinement
$\Delta\rho_{max}$, $\Delta\rho_{min}$ (e Å^{-3})	0.28, −0.42
Absolute structure	Hooft *et al.* (2010)
Absolute structure parameter	−0.04 (6)

Computer programs: *APEX3* (Bruker, 2016), *SAINT* (Bruker, 2016), *SHELXT* (Sheldrick, 2015*a*), *PLATON* (Spek, 2020), *ORTEP-3 for Windows* (Farrugia, 2012), *Mercury* (Macrae *et al.*, 2020), *olex2.refine* (Bourhis *et al.*, 2015), *SHELXL* (Sheldrick, 2015*b*) and *OLEX2* (Dolomanov *et al.*, 2009).

environment, limiting enantioselective or diastereoselective outcomes during reactions (Gallou & Senanayake, 2006).

Drug hydrolysis plays a crucial role in pharmaceutical research, as it directly affects the stability, efficacy and safety of drug formulations (Mehta & Bhayani, 2017). This chemical process, which involves breaking down drug molecules through a reaction with water, is a common pathway for drug degradation (Lieberman & Vemuri, 2015). In addition to water, solvents such as alcohols and other organic solvents can also influence drug hydrolysis (Mehta & Bhayani, 2017). These solvents may act as reactants or catalysts (Dutta *et al.*, 2024) in hydrolytic reactions, depending on the chemical nature of the drug and the solvent environment. Hydrolysis can affect various functional groups in drug molecules, such as esters, amides and lactones, leading to therapeutic effectiveness and potential toxicity changes (Zhou *et al.*, 2017). In certain instances, alcohols can engage in transesterification reactions, where an ester group in the drug molecule interacts with the alcohol to create a new ester (Lieberman & Vemuri, 2015). This reaction is particularly relevant in formulations that include ethanol or other alcohols as solvents. Solvents like acetone, dimethyl sulfoxide (DMSO) or acetonitrile can alter the reaction kinetics of hydrolysis. They may stabilize or destabilize intermediates, thereby impacting the rate of hydrolysis (Schmidt & Scholze, 1985; Issa & Luyt, 2019). The presence of both water and organic solvents can create unique environments that affect hydrolysis.

In recent years, advances in various analytical techniques, such as high-performance liquid chromatography (HPLC), have enhanced our ability to study hydrolytic degradation and predict its impact on drug stability (Battu & Pottabathini, 2015). Researchers are also exploring innovative formulation strategies, including the use of excipients and encapsulation methods, to mitigate hydrolysis and extend the shelf life of pharmaceutical products. Understanding the mechanisms and factors influencing hydrolysis remains a critical area of focus, as it informs the development of more stable and effective drug formulations.

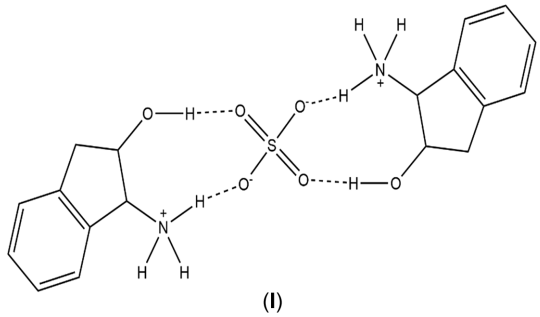

(**I**)
Scheme 1

2. Experimental

2.1. Synthesis and crystallization

The one-pot synthesis reflux method (Smith *et al.*, 2015) was used for the synthesis of bis(2-hydroxy-2,3-dihydro-1*H*-inden-1-aminium) sulfate, (**I**) (Scheme 1). In a dram vial, 0.020 g of indinavir sulfate (0.0324 mmol) was dissolved in 1-propanol solvent and heated at 363 K while stirring at 300 rpm for 4 h. With the lid of the dram vial loosely open, the solution was allowed to evaporate slowly at temperatures ranging from 283 to 273 K. After three weeks, colourless plates had formed.

2.2. Refinement

Crystal data, data collection and structure refinement details are summarized in Table 1. H atoms on O and N atoms were allowed to refine freely.

2.3. Surface analyses

Hirshfeld surface analysis was performed to quantify the various intermolecular interactions contributing to the crystal structure of salt (**I**) using *CrystalExplorer* (Version 17.5; Spackman *et al.*, 2021). A surface was mapped over d_{norm}, along with two-dimensional (2D) fingerprint plots, which were utilized to analyse these interactions (McKinnon *et al.*, 2007; Spackman & Jayatilaka, 2009). The Hirshfeld surface of salt (**I**) is colour-coded and mapped over d_{norm}. The surface area, density and volumetric analyses were conducted using the two-probe mode configuration, employing a small radius probe (r_{small_p}) of 1.2 Å and a large radius probe (r_{large_p}) of 3.0 Å. Optimization was performed to a depth of 4, with a grid

resolution of 0.2 Å for enhanced accuracy using *MoloVol* (Version 1.1.1; Maglic & Lavendomme, 2022).

2.4. Fourier transform IR (FT–IR) spectroscopy and Raman spectroscopy

FT–IR analysis was performed at 288 K using a Shimadzu QATR10 ATR accessory with a germanium crystal. Measurements were taken in percentage transmittance mode with 64 scans, a resolution of 4 cm^{-1} and a range of 700–4.000 cm^{-1}. Data were processed with *LabSolutions IR* (Version 2.26). Raman spectroscopy utilized a Bruker MultiRam Fourier transform spectrometer with a Nd-YAG laser and a germanium diode detector, also with 64 scans at 450 mW power.

2.5. Thermogravimetric analysis (TGA) and differential scanning calorimetry (DSC)

Thermogravimetric analysis and differential scanning calorimetry data were collected using a thermogravimetric analyser from an Advanced Laboratory Solutions (TGA/DSC) SQ600 between 323 and 1073 K, at a heating rate of 283 K min^{-1} and a nitrogen gas flow rate of 20 ml min^{-1}.

2.6. Nuclear magnetic resonance (NMR)

For the NMR analysis, crystals of salt (**I**) were dissolved in deuterated DMSO-d_6 containing 1% tetramethylsilane and transferred to an NMR tube for analysis. The samples were analysed using an Agilent 500 MHz spectrometer at room temperature (299 K) and the NMR spectra were captured (^{1}H at 500 MHz and ^{13}C at 125 MHz).

^{1}H NMR (500 MHz, DMSO-d_6): δ (ppm) 8.50 (*s*, 1H, $-NH_3$), 8.15 (*s*, 1H, $-NH_3$), 7.71 (*s*, 1H, $-NH_3$), 7.48–7.23 (*m*, 4H, –CH aromatic of the indenol moiety), 5.85 (*s*, 1H, OH), 4.57 [*d*, 1H, –CH(OH)], 3.02–2.98 (*m*, 1H, $-CH_2$), 2.95–2.91 (*m*, 1H, $-CH_2$). ^{13}C NMR (125 MHz, DMSO-d_6): δ (ppm) 141.40 (1C), 138.62 (1C), 129.13 (1C), 128.85 (2C), 126.77 (1C), 70.17 (1C), 62.44 (1C), 35.53 (1C). HRMS–ESI (acetonitrile, *m*/*z*) calculated for $[C_9H_{12}NO]^+$ 150.09; found: $[M+2]^+$ 152.2306.

3. Results and discussion

Indinavir sulfate was reacted with 1-propanol, which resulted in the alcoholysis of the salt into two distinct parts. Under certain stress conditions, such as changes in pH, temperature and oxidation, indinavir sulfate is known to hydrolyse and ultimately degrade (Rao *et al.*, 2013), as observed in the cleavage of the molecule. However, since 1-propanol is an alcohol, the degradation of indinavir sulfate in this case is referred to as alcoholysis. A reaction where an alcohol molecule acts as a reactant, breaking chemical bonds, typically in esters or similar compounds, by replacing certain functional groups with an alcohol group (Avhad & Marchetti, 2015). The compound cleaved into (3*S*,5*S*)-3-benzyl-5-[(2-{[(*tert*-butylamino)oxy]methyl}-4-(pyridin-3-ylmethyl)piperazin-1-yl)methyl]-dihydrofuran-2(3*H*)-one, which remained in solution, and the salt bis(2-hydroxy-2,3-dihydro-1*H*-inden-1-aminium) sulfate, (**I**) (Scheme 1), which was crystallized.

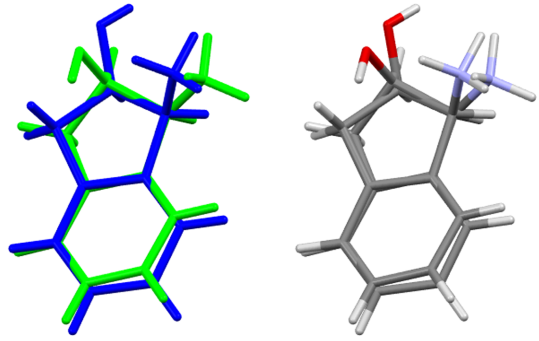

Figure 1
Molecular overlay of the 2-hydroxy-2,3-dihydro-1*H*-inden-1-aminium cations, highlighting their minor conformational diversity.

Salt (**I**) crystallized in the monoclinic space group $P2_1$ with $Z = 2$. The proposed chemical formula for the asymmetric unit is $2C_9H_{12}NO^+\cdot SO_4^{2-}$. The cations are, however, slightly different from one another due to the absence of a centre of inversion, indicating that the cations themselves are not symmetrical. The cations exhibit minor conformational diversity. The hydroxy H atoms point in opposite directions, at an angle of 138° from one another (Fig. 1).

The asymmetric unit of salt (**I**) is illustrated in Fig. 2. The figure illustrates that the salt is stabilized by hydrogen bonds, with donor–acceptor distances ranging from 2.6 to 2.9 Å. Both amine functional groups of the cations interact with the S═O bonds: N1···O5 exhibits a hydrogen-bond length of 2.807 (4) Å, while N2···O6 displays a length of 2.833 (3) Å.

Additionally, the alcohol functional groups form hydrogen bonds with the S═O moieties. Specifically, O1···O3 features a hydrogen-bond length of 2.724 (3) Å and O2···O4 forms a hydrogen bond of 2.675 (3) Å. The bond angles observed in these interactions are linked to the sulfate anion. The out-of-plane bond angle for C9—C1—O1 is 112.5 (3)°, while the second cation exhibits a corresponding bond angle for C11—C10—O2 of 113.3 (3)°. Positioned between the two cations, the sulfate anion adopts a tetrahedral structure with an average O—S—O bond angle of 109.42°. This configuration

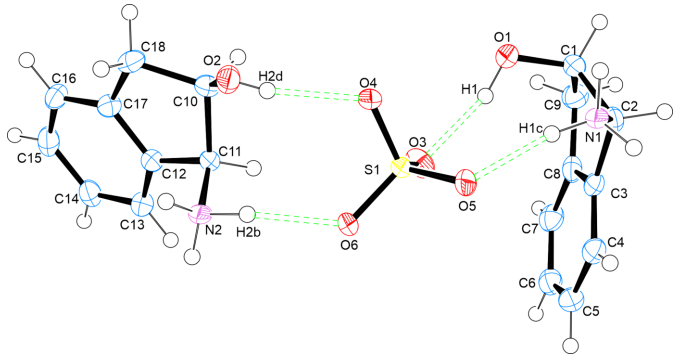

Figure 2
The asymmetric unit of salt (**I**). Displacement ellipsoids are drawn at the 50% probability level.

Table 2
Selected bond angles (°).

O4—S1—O3	110.40 (14)	O6—S1—O3	110.36 (13)
O5—S1—O3	110.40 (13)	O6—S1—O4	108.23 (13)
O5—S1—O4	108.36 (14)	O6—S1—O5	109.02 (13)

is characteristic of tetrahedral molecules and reflects the optimized molecular geometry within the crystal lattice. The bond angles for the sulfate anion are detailed in Table 2.

Hirshfeld surface analysis was conducted to characterize the intermolecular interactions between each independent cation and the sulfate ion within the asymmetric unit. The molecular assembly is inherently asymmetric, highlighting the noncentrosymmetric nature of the structure. The two-dimensional (2D) fingerprint plots were generated based solely on the asymmetric unit rather than the full packing arrangement within the unit cell ($Z = 2$), ensuring an accurate depiction of the local interaction motifs rather than global lattice effects (Fig. 3). The red areas between the aminium and sulfate ions, as well as between the hydroxy groups and sulfate ions, indicate short intermolecular bonds, such as strong hydrogen bonding and van der Waals interactions, due to the distance between bonds. The blue spots indicate regions in the crystal where the contacts between the atoms are larger than the sum of the van der Waals radii. These contacts are typically weak interactions that contribute to less significant intermolecular bonding.

In the first independent cation (Fig. 3, left), the dominance of O···H/H···O interactions at 41.0% aligns with their significant role in hydrogen bonding, which often drives molecular stability. The closely following H···H interactions (40.1%) highlight the contribution of van der Waals forces in stabilizing the system. C···H/H···C contacts (18.1%) suggest secondary interactions, possibly contributing to the overall packing and orientation of the components. Finally, the minimal C···O/O···C interactions at 0.8% imply that these interactions play a very limited role in the stability of the system (Fig. 4).

In the second independent cation (Fig. 3, right), the interactions within the crystal structure indicate an increase in H···H contacts to 45.2%, underscoring their dominant role,

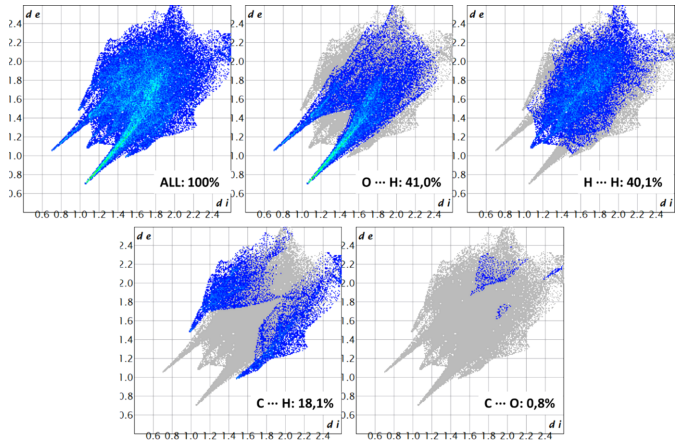

Figure 4
2D fingerprint plots of cation *A* of salt (**I**), detailing the intramolecular interactions.

likely reflecting stronger van der Waals interactions or a more densely packed molecular environment. The similar percentages of the O···H/H···O interactions at 44.4% highlights the significance of hydrogen bonding, potentially linked to stability or reactivity differences compared to the first part of the structure. The lower proportion of C···H/H···C interactions at 10.3% suggests interaction variations due to the change in molecular orientation. These changes offer insights into differing behaviour pathways across structural regions. C···O interactions remain minor, making up just 0.8% here as well (Fig. 5).

This consistency across both parts of the crystal structure suggests that C···O contacts have a limited role in stabilizing the molecular framework. However, even such low percentages can occasionally hint at subtle but specific interactions, such as dipole–dipole alignments or lone-pair contributions.

Further crystallographic details revealed that the calculated density of the crystal is $\rho = 1.408$ Mg m^{-3}. The total molecular volume of the unit cell was measured at 934.95 Å^3, with van der Waals volumes accounting for 71.43% of the cell, while 28.57% corresponded to probe-excluded void volumes, according to the *MoloVol* volumetric analysis. The calculated van der Waals surface area of the molecule is 687.30 Å^2

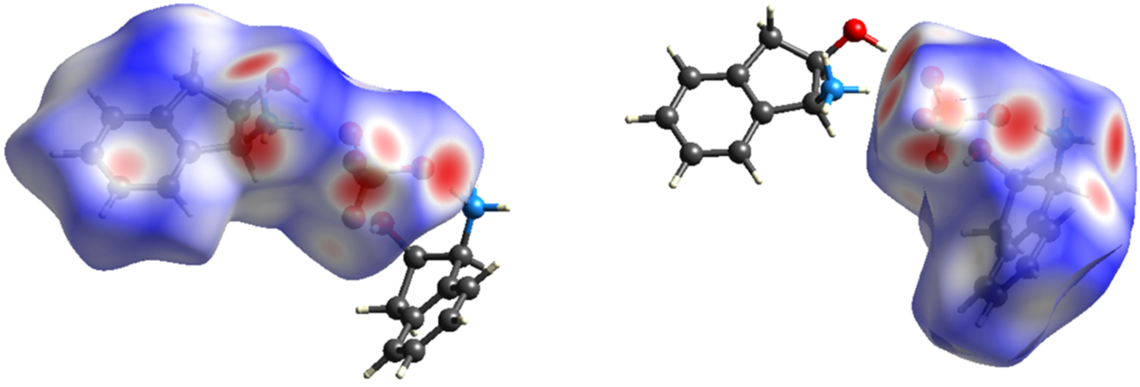

Figure 3
Two views of the independent cation surfaces of the salt (**I**) mapped over d_{norm}, indicating the various intermolecular bonds in white, red and blue.

Table 3
FT–IR spectral data analysis of (**I**).

Group	Wavenumber observed (cm^{-1})	Wavenumber (cm^{-1})	Intensity	Assignment
$–NH_2$	2995–2849	3200–3180	Strong	NH_2 primary amine
–OH	3003–2868	3100–2400	Very strong	OH stretch, very broad band
$–NH_2$	1650	1650–1580	Mid-strength	NH_2 deformation
S═O	1038	1060–1045	Very strong	S═O stretch

Table 4
Raman spectral data analysis of (**I**).

Group	Wavenumber observed (cm^{-1})	Wavenumber (cm^{-1})	Intensity	Assignment
$–NH_3^+$	3065	3200 – 3100	Strong	N—H stretch
C—H	2935/2905	3000–2800	Very strong	Aliphatic C—H stretching
C═C	1615/1590	1650–1580	Strong	C═C aromatic ring stretch
C—H	1460	1500–1300	Mid-strength	C—H deformation
S═O	1025–990	1100–980	Strong	S═O symmetric/asymmetric stretching
SO_4^{2-}	790–730	750–600	Mid-strength	SO_4^{2-} bending deformation

(Fig. 6) and is solely based on the van der Waals radii of the constituent atoms (Charry & Tkatchenko, 2024). The calculated van der Waals surface area of 687.30 $Å^2$ reflects the size and shape of the molecular envelope over which intermolecular interactions occur. When considered alongside the Hirshfeld surface interaction percentages, this surface area indicates that there is sufficient contact area to support both dense molecular packing, as evidenced by the high proportion of H···H contacts, and extensive hydrogen bonding, as seen in the O···H/H···O contributions. This analysis highlights the spatial distribution of close contacts and underscores the dual role of van der Waals forces and hydrogen bonding in stabilizing the crystal structure.

The degradation product, (1*S*,2*R*)-(+)-*cis*-1-amino-2-indanol, formed by alcoholysis of the amide bond on indinavir, is enantiopure and lacks inversion symmetry. This intrinsic chirality drives the selection of space group $P2_1$, as centrosymmetric packing would require both enantiomers, which are absent in this case. Furthermore, the sulfate ion plays a crucial role in stabilizing the asymmetric molecular arrangement. The anion engages in specific hydrogen-bonding and electrostatic interactions, which reinforce the observed packing mode.

The FT–IR and Raman spectra of salt (**I**) are depicted in Fig. 7, and the major peaks are summarized in Table 3. The strong peak at 2995–2849 cm^{-1} depicts a primary amine peak at 3180–3200 cm^{-1}. A 3003–2868 cm^{-1} peak was recorded, which is observed as a symmetric vibration with another $–NH_3^+$ group at 1650–1580 cm^{-1}. The very strong and broad peak at 3100–2400 cm^{-1} indicates the presence of –OH groups. In the range 1060–1045 cm^{-1}, there is an S═O stretch, depicted as a very strong peak in the fingerprint region. There is an additional peak that was observed at 1765 cm^{-1}, which corresponds with an S═O stretching vibration. The high polarity of S═O leads to a significant change in the dipole moment during the stretching vibration that would appear in the FT–IR spectra. The same distinctive peak may appear smaller on the Raman spectra due to the polarization change during the vibration. The peak which appears on the FT–IR spectrum at

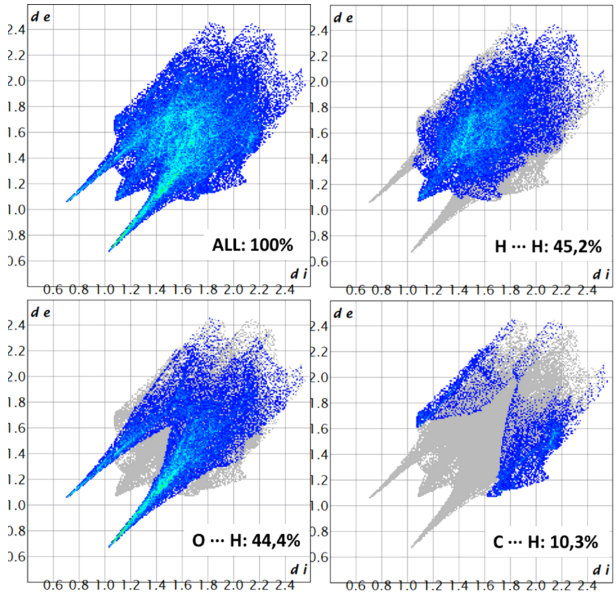

Figure 5
2D fingerprint plots of cation *B* of salt (**I**), detailing the intramolecular interactions.

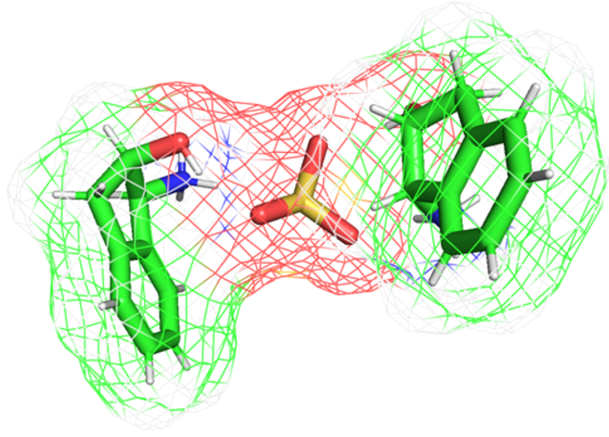

Figure 6
The van der Waals surface area map of the asymmetric unit of salt (**I**).

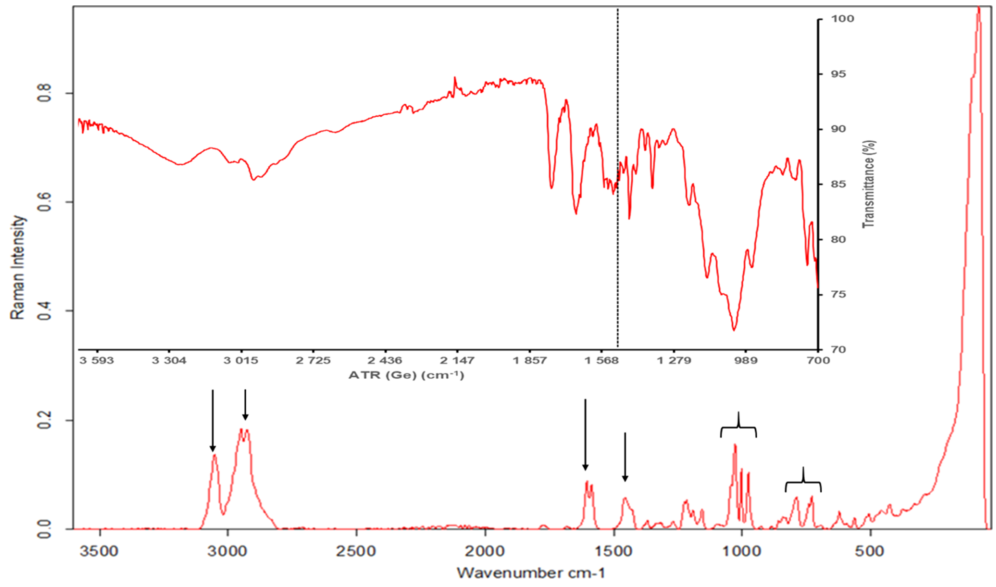

Figure 7
Figure 7: Superimposed FT–IR and Raman spectra of salt (**I**), with arrows indicating major peaks observed in the Raman spectrum.

1700–1800 cm^{-1} is due to the asymmetric stretch, which was observed on S═O, whereas the vibration observed at 1045–1060 cm^{-1} is due to S═O being observed as a symmetric stretching vibration.

Raman spectroscopy of compound (**I**) revealed characteristic vibrational modes consistent with its functional groups as summarized in Table 4. A strong band at 3065 cm^{-1} corresponds to N—H stretching of the protonated amine ($–NH_3^+$) groups, while very strong peaks at 2935 and 2905 cm^{-1} arise from aliphatic C—H stretching. Aromatic ring C═C stretching modes appear at 1615 and 1590 cm^{-1}. A medium-intensity band at 1460 cm^{-1} is attributed to C—H bending vibrations. Strong bands in the 1025–990 cm^{-1} region correspond to symmetric and asymmetric S═O stretching of the sulfate anion, and medium-intensity peaks at 790–730 cm^{-1} are assigned to SO_4^{2-} bending deformations, consistent with typical tetrahedral sulfate vibrational behaviour.

Thermogravimetric analysis (TGA) and differential scanning calorimetry (DSC) were used to investigate the thermal behaviour of salt (**I**). The TGA data show a gradual decrease in weight from about 200 °C, indicating the onset of thermal decomposition. Although no distinct inflexion is observed below 200 °C, a slight drift in the baseline of the derivative thermogravimetric (DTG) curve may suggest minor desorption of surface-bound solvent or water in that region. This is supported by the DSC trace, which displays a shallow endothermic event in the same range, consistent with solvent loss rather than melting.

Notably, a well-defined melting endotherm is absent, confirming that salt (**I**) does not exhibit a simple melting transition under these conditions. With further heating, an exothermic transition is observed at approximately 306.6 °C (579.75 K), which likely marks the beginning of decomposition (possibly involving the loss of the $C_{18}H_{24}N_2O_2$ fragments). The thermal event observed near 325–350 °C indicates the total decomposition of the sulfate SO_4^{2-} anion (Brown, 1988). Fig. 8 illustrates these thermal events, where the initial weight loss and corresponding endothermic DSC feature collectively

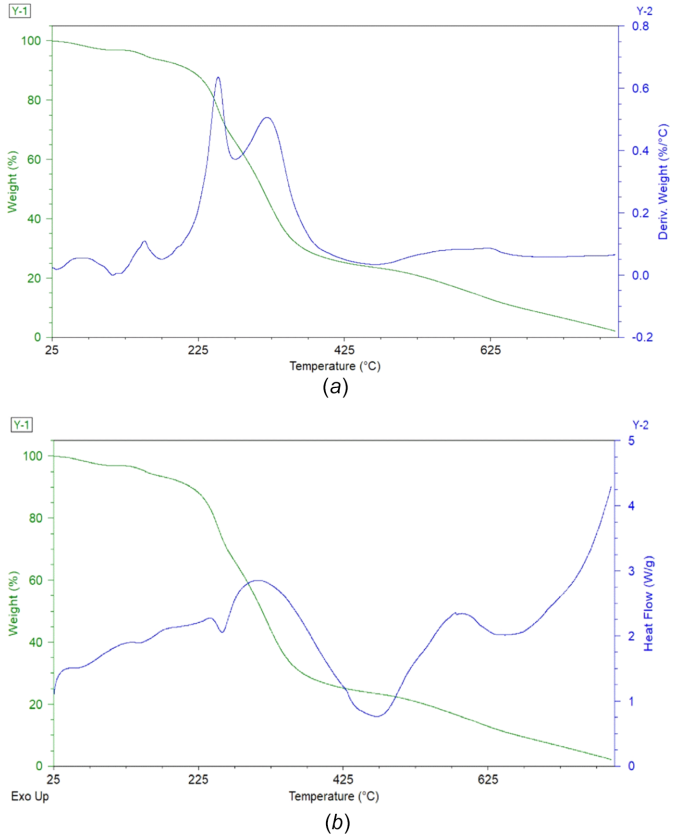

Figure 8
(*a*) TGA–DTG data and (*b*) TGA–DSC data, indicating a mass loss due to the decomposition of the sulfate anion and the 2-hydroxy-2,3-dihydro-1*H*-inden-1-aminium cation.

emphasize the removal of residual solvent/moisture, with later peaks arising from compound degradation rather than phase transitions.

The ^{1}H NMR exhibits multiplet signals at δ 2.91 to 2.95 ppm and δ 3.00 to 3.03 ppm due to the aliphatic protons of CH_2. The OH group produced a single broad peak at δ 5.83 ppm. A doublet was observed because of one CH(OH) proton. The four protons on the indenol aromatic ring were responsible for the multiplet that was observed. At δ 8.50, 8.13 and 7.71, three single peaks were observed due to the NH_3 protons.

In the ^{13}C NMR spectral analysis, the aliphatic region shows the signal due to CH_2 at δ 35.53 ppm, while the second aliphatic carbon signal due to C—NH_3 appears at δ 62.44 ppm. The third aliphatic carbon signal is due to CH(OH) at δ 70.17 ppm. A signal due to one carbon at δ 126.77 ppm was observed. Another signal due to the two aromatic carbons of the indenol moiety was observed at δ 128.85 ppm. At δ 129.13 ppm, a signal due to one carbon (–CH) on the aromatic region was observed. A signal due to –C(CH)═ was observed at δ 138.62 ppm. A signal due to the carbon in the aromatic ring was observed at δ 141.40 ppm.

Funding information

Funding for this research was provided by: National Research Foundation (grant No. CSUR23042597072 to Mark G. Smith).

References

Avhad, M. R. & Marchetti, J. M. (2015). *Renew. Sustain. Energy Rev.* **50**, 696–718.
Battu, S. & Pottabathini, V. (2015). *Am. J. Anal. Chem.* **6**, 145–155.
Bourhis, L. J., Dolomanov, O. V., Gildea, R. J., Howard, J. A. K. & Puschmann, H. (2015). *Acta Cryst.* A**71**, 59–75.
Brown, M. E. (1988). *Introduction to thermal analysis: techniques and applications*, p. 20. London, New York: Chapman and Hall.
Bruker (2016). *APEX3*, *SAINT-Plus* and *SADABS*. Bruker AXS Inc., Madison, Wisconsin, USA.
Charry, J. & Tkatchenko, A. (2024). *J. Chem. Theory Comput.* **20**, 7469–7478.
Dolomanov, O. V., Bourhis, L. J., Gildea, R. J., Howard, J. A. K. & Puschmann, H. (2009). *J. Appl. Cryst.* **42**, 339–341.
Dorsey, B. D., Levin, R. B., McDaniel, S. L., Vacca, J. P., Guare, J. P., Darke, P. L., Zugay, J. A., Emini, E. A., Schleif, W. A., Quintero, J. C., Lin, J. H., Chen, I.-W., Holloway, M. K., Fitzgerald, P. M. D., Axwl, M. G., Ostovic, D., Anderson, P. S. & Huff, J. R. (1994). *J. Med. Chem.* **37**, 3443–3451.
Dutta, S., Zhang, Q., Yu, I. K. M. & Tsang, D. C. W. (2024). *ACS Sustain. Chem. Eng.* **12**, 9222–9230.
Farrugia, L. J. (2012). *J. Appl. Cryst.* **45**, 849–854.
Gallou, I. & Senanayake, C. (2006). *Chem. Rev.* **106**, 2843–2874.
Hooft, R. W. W., Straver, L. H. & Spek, A. L. (2010). *J. Appl. Cryst.* **43**, 665–668.
Issa, A. A. & Luyt, A. S. (2019). *Polymers* **11**, 537.
Lieberman, H. & Vemuri, N. M. (2015). *The practice of medicinal chemistry*, pp. 767–791. New York: Academic Press.
Macrae, C. F., Sovago, I., Cottrell, S. J., Galek, P. T. A., McCabe, P., Pidcock, E., Platings, M., Shields, G. P., Stevens, J. S., Towler, M. & Wood, P. A. (2020). *J. Appl. Cryst.* **53**, 226–235.
Maglic, J. B. & Lavendomme, R. (2022). *J. Appl. Cryst.* **55**, 1033–1044.
Matamoros, E., Light, M. E., Cintas, P. & Palacios, J. C. (2023). *Molecules* **28**, 1670.
McKinnon, J. J., Jayatilaka, D. & Spackman, M. A. (2007). *Chem. Commun.* pp. 3814–3816.
Mehta, P. & Bhayani, D. (2017). *J. Pharm. Biomed. Anal.* **136**, 111–119.
Rao, R. N., Raju, S. S. & Vali, R. M. (2013). *J. Chromatogr. B* **931**, 174–180.
Schmidt, H. & Scholze, H. (1985). *Mechanisms and kinetics of the hydrolysis and condensation of alkoxides*, in *Glass . . . current issues*, edited by A. F. Wright & J. Dupuy. NATO ASI Series, Vol 92. Dordrecht: Springer.
Sheldrick, G. M. (2015*a*). *Acta Cryst.* A**71**, 3–8.
Sheldrick, G. M. (2015*b*). *Acta Cryst.* C**71**, 3–8.
Smith, M. G., Forbes, R. P. & Lemmerer, A. (2015). *Cryst. Growth Des.* **15**, 3813–3821.
Spackman, M. A. & Jayatilaka, D. (2009). *CrystEngComm* **11**, 19–32.
Spackman, P. R., Turner, M. J., McKinnon, J. J., Wolff, S. K., Grimwood, D. J., Jayatilaka, D. & Spackman, M. A. (2021). *J. Appl. Cryst.* **54**, 1006–1011.
Spek, A. L. (2020). *Acta Cryst.* E**76**, 1–11.
Zhou, D., Porter, W. R. & Zhang, G. G. Z. (2017). *Drug stability and degradation studies*, in *Developing solid oral dosage forms*, 2nd ed., edited by Y. Qiu, Y. Chen, G. G. Z. Zhang, L. Yu & R. V. Mantri, ch. 5, pp. 113–149. New York: Academic Press.

supporting information

Acta Cryst. (2025). C**81** [https://doi.org/10.1107/S2053229625005807]

The cleavage of indinavir sulfate: synthesis and characterization of a *cis*-1-amino-2-indanol salt

Tebogo M. L. Mokoto, Andreas Lemmerer, Yasien Sayed, Kgaugelo C. Tapala, Itumeleng B. Setshedi and Mark G. Smith

Computing details

Bis(2-hydroxy-2,3-dihydro-1*H*-inden-1-aminium) sulfate

Crystal data

$2C_9H_{12}NO^+·SO_4^{2-}$
M_r = 396.47
Monoclinic, $P2_1$
a = 11.6412 (10) Å
b = 6.4226 (4) Å
c = 12.8761 (10) Å
β = 103.791 (4)°
V = 934.95 (12) Å^3
Z = 2
$F(000)$ = 420.538
D_x = 1.408 Mg m^{-3}
Mo $K\alpha$ radiation, λ = 0.71073 Å
Cell parameters from 5055 reflections
θ = 2.7–24.9°
μ = 0.21 mm^{-1}
T = 123 K
Plate, colourless
0.57 × 0.11 × 0.03 mm

Data collection

Bruker APEXII CCD diffractometer
φ and ω scans
26758 measured reflections
3458 independent reflections
2956 reflections with $I \geq 2u(I)$
R_{int} = 0.098
θ_{max} = 25.5°, θ_{min} = 1.6°
h = −14→14
k = −7→7
l = −15→15

Refinement

Refinement on F^2
Least-squares matrix: full
$R[F^2 > 2\sigma(F^2)]$ = 0.045
$wR(F^2)$ = 0.111
S = 1.04
3454 reflections
276 parameters
1 restraint
30 constraints
H atoms treated by a mixture of independent and constrained refinement
$w = 1/[\sigma^2(F_o^2) + (0.0624P)^2 + 0.1242P]$ where $P = (F_o^2 + 2F_c^2)/3$
$(\Delta/\sigma)_{max}$ = 0.0004
$\Delta\rho_{max}$ = 0.28 e Å^{-3}
$\Delta\rho_{min}$ = −0.42 e Å^{-3}
Absolute structure: Hooft *et al.* (2010)
Absolute structure parameter: −0.04 (6)

Special details

Refinement. Data for the crystal was collected using a Bruker Apex II CCD area diffractometer with monochromated Mo-Kα radiation (λ = 0.71073) at a temperature of 123K. The collection method employed ω-scans with a 0.5° width. Subsequently, the data was reduced using SAINT+ version 6.02 software (Bruker, 2012), and empirical absorption corrections were applied using SADABS (Bruker, 2012). All diagrams intended for publication were prepared using ORTEP (Farrugia, 2012), WinGX (Farrugia, 2012), MERCURY (Macrae *et al.*, 2006), and PLATON (Spek, 2009).

Fractional atomic coordinates and isotropic or equivalent isotropic displacement parameters (Å²)

	x	*y*	*z*	U_{iso}*/U_{eq}
O1	0.7936 (2)	1.0818 (3)	0.38783 (16)	0.0265 (5)
H1b	0.594 (3)	1.275 (6)	0.431 (3)	0.024 (9)*
H1c	0.585 (5)	1.047 (10)	0.442 (4)	0.086 (18)*
H1d	0.553 (3)	1.187 (6)	0.529 (3)	0.037 (10)*
H2a	0.592 (3)	0.042 (5)	0.189 (2)	0.013 (8)*
H2b	0.558 (4)	0.268 (7)	0.194 (3)	0.044 (11)*
H2c	0.530 (4)	0.146 (9)	0.087 (4)	0.066 (14)*
H2d	0.572 (3)	0.576 (6)	0.095 (3)	0.024 (10)*
H1	0.786 (4)	0.948 (8)	0.404 (3)	0.044 (11)*
C1	0.8261 (3)	1.1962 (5)	0.4848 (2)	0.0245 (7)
H1a	0.8382 (3)	1.3461 (5)	0.4693 (2)	0.0294 (8)*
C2	0.7316 (2)	1.1760 (5)	0.5504 (2)	0.0218 (6)
H2	0.7384 (2)	1.2975 (5)	0.6001 (2)	0.0262 (7)*
C3	0.7679 (3)	0.9820 (5)	0.6147 (2)	0.0232 (7)
C4	0.7001 (3)	0.8483 (5)	0.6597 (2)	0.0275 (7)
H4	0.6188 (3)	0.8765 (5)	0.6546 (2)	0.0330 (9)*
C5	0.7531 (3)	0.6727 (6)	0.7123 (2)	0.0293 (7)
H5	0.7078 (3)	0.5791 (6)	0.7435 (2)	0.0352 (8)*
C6	0.8717 (3)	0.6319 (5)	0.7198 (2)	0.0313 (8)
H6	0.9066 (3)	0.5099 (5)	0.7556 (2)	0.0376 (9)*
C7	0.9404 (3)	0.7674 (5)	0.6755 (3)	0.0309 (8)
H7	1.0221 (3)	0.7401 (5)	0.6822 (3)	0.0370 (9)*
C8	0.8878 (3)	0.9428 (5)	0.6216 (2)	0.0257 (7)
C9	0.9374 (3)	1.1088 (5)	0.5613 (3)	0.0301 (8)
H9a	0.9923 (3)	1.0482 (5)	0.5215 (3)	0.0361 (10)*
H9b	0.9792 (3)	1.2179 (5)	0.6104 (3)	0.0361 (10)*
C10	0.6832 (3)	0.4211 (5)	0.0559 (2)	0.0267 (7)
H10	0.7475 (3)	0.5271 (5)	0.0766 (2)	0.0321 (8)*
C11	0.7036 (3)	0.2466 (5)	0.1412 (2)	0.0215 (6)
H11	0.7500 (3)	0.3013 (5)	0.2114 (2)	0.0257 (8)*
C12	0.7761 (3)	0.0899 (5)	0.0968 (2)	0.0242 (7)
C13	0.8438 (3)	−0.0711 (5)	0.1504 (3)	0.0269 (7)
H13	0.8465 (3)	−0.0978 (5)	0.2235 (3)	0.0323 (8)*
C14	0.9079 (3)	−0.1939 (5)	0.0948 (3)	0.0292 (8)
H14	0.9552 (3)	−0.3051 (5)	0.1304 (3)	0.0350 (9)*
C15	0.9032 (3)	−0.1548 (5)	−0.0121 (3)	0.0315 (8)
H15	0.9473 (3)	−0.2395 (5)	−0.0492 (3)	0.0378 (9)*
C16	0.8346 (3)	0.0073 (5)	−0.0655 (3)	0.0295 (8)

H16	0.8313 (3)	0.0334 (5)	−0.1387 (3)	0.0354 (9)*
C17	0.7709 (3)	0.1308 (5)	−0.0105 (2)	0.0253 (7)
C18	0.6934 (3)	0.3153 (5)	−0.0490 (3)	0.0294 (8)
H18a	0.6148 (3)	0.2712 (5)	−0.0919 (3)	0.0353 (9)*
H18b	0.7303 (3)	0.4094 (5)	−0.0926 (3)	0.0353 (9)*
N1	0.6093 (2)	1.1668 (5)	0.48267 (19)	0.0210 (5)
N2	0.5885 (2)	0.1581 (5)	0.1530 (2)	0.0222 (5)
O2	0.5714 (2)	0.5222 (3)	0.04280 (19)	0.0298 (6)
O3	0.73413 (19)	0.6714 (4)	0.38608 (17)	0.0318 (5)
O4	0.5968 (2)	0.7545 (3)	0.21921 (17)	0.0269 (5)
O5	0.5353 (2)	0.7843 (3)	0.38358 (18)	0.0286 (5)
O6	0.5679 (2)	0.4458 (3)	0.31437 (16)	0.0238 (5)
S1	0.61026 (7)	0.66412 (11)	0.32677 (5)	0.02110 (18)

Atomic displacement parameters (Å²)

	U^{11}	U^{22}	U^{33}	U^{12}	U^{13}	U^{23}
O1	0.0363 (14)	0.0236 (12)	0.0208 (11)	0.0005 (9)	0.0091 (10)	−0.0004 (9)
C1	0.0306 (17)	0.0192 (17)	0.0259 (15)	0.0010 (12)	0.0109 (13)	0.0007 (12)
C2	0.0258 (16)	0.0180 (14)	0.0212 (14)	−0.0013 (14)	0.0046 (12)	−0.0052 (14)
C3	0.0313 (18)	0.0234 (17)	0.0144 (14)	0.0002 (13)	0.0046 (13)	−0.0023 (12)
C4	0.035 (2)	0.0273 (17)	0.0209 (16)	0.0013 (14)	0.0071 (14)	−0.0012 (13)
C5	0.0391 (19)	0.0262 (16)	0.0227 (14)	−0.0004 (17)	0.0074 (13)	0.0021 (16)
C6	0.045 (2)	0.0260 (19)	0.0208 (15)	0.0054 (15)	0.0041 (14)	0.0008 (13)
C7	0.035 (2)	0.0338 (18)	0.0221 (16)	0.0067 (15)	0.0034 (14)	0.0004 (14)
C8	0.0309 (18)	0.0238 (16)	0.0215 (15)	0.0059 (14)	0.0048 (13)	−0.0048 (13)
C9	0.033 (2)	0.031 (2)	0.0263 (16)	−0.0015 (13)	0.0059 (14)	0.0016 (12)
C10	0.037 (2)	0.0190 (15)	0.0229 (16)	−0.0008 (14)	0.0057 (14)	0.0033 (13)
C11	0.0303 (17)	0.0161 (14)	0.0177 (15)	−0.0024 (12)	0.0052 (13)	−0.0002 (12)
C12	0.0297 (19)	0.0216 (16)	0.0232 (15)	−0.0046 (12)	0.0097 (14)	−0.0023 (12)
C13	0.0315 (18)	0.0258 (17)	0.0246 (16)	−0.0013 (14)	0.0091 (13)	−0.0026 (13)
C14	0.0321 (19)	0.0236 (18)	0.0319 (18)	−0.0013 (13)	0.0080 (15)	−0.0060 (13)
C15	0.0300 (19)	0.0336 (18)	0.0327 (19)	−0.0053 (15)	0.0111 (15)	−0.0129 (15)
C16	0.036 (2)	0.0335 (19)	0.0218 (16)	−0.0059 (15)	0.0122 (15)	−0.0051 (13)
C17	0.0285 (17)	0.0256 (18)	0.0230 (15)	−0.0039 (14)	0.0087 (13)	−0.0002 (13)
C18	0.039 (2)	0.0298 (18)	0.0202 (16)	0.0014 (15)	0.0084 (15)	0.0060 (13)
N1	0.0272 (13)	0.0178 (12)	0.0189 (12)	0.0015 (13)	0.0075 (10)	0.0032 (13)
N2	0.0333 (15)	0.0152 (12)	0.0193 (12)	0.0019 (13)	0.0084 (11)	0.0042 (13)
O2	0.0435 (16)	0.0236 (12)	0.0207 (12)	0.0048 (10)	0.0046 (11)	−0.0012 (10)
O3	0.0278 (12)	0.0246 (11)	0.0375 (12)	−0.0004 (11)	−0.0026 (9)	0.0000 (12)
O4	0.0449 (15)	0.0175 (10)	0.0187 (11)	−0.0028 (10)	0.0084 (10)	0.0025 (8)
O5	0.0406 (14)	0.0203 (12)	0.0310 (12)	−0.0007 (10)	0.0202 (11)	−0.0059 (9)
O6	0.0365 (13)	0.0144 (10)	0.0219 (11)	−0.0019 (9)	0.0099 (9)	−0.0025 (9)
S1	0.0322 (4)	0.0147 (3)	0.0176 (3)	−0.0003 (3)	0.0083 (3)	0.0002 (3)

Geometric parameters (Å, º)

O1—H1	0.89 (5)	C9—H9a	0.9900
O1—C1	1.420 (4)	C9—H9b	0.9900
H1b—N1	0.95 (4)	C10—H10	1.0000
H1c—N1	0.93 (6)	C10—C11	1.548 (4)
H1d—N1	1.00 (4)	C10—C18	1.542 (4)
H2a—N2	0.87 (4)	C10—O2	1.427 (4)
H2b—N2	0.99 (4)	C11—H11	1.0000
H2c—N2	0.96 (5)	C11—C12	1.510 (4)
H2d—O2	0.76 (3)	C11—N2	1.496 (4)
C1—H1a	1.0000	C12—C13	1.381 (4)
C1—C2	1.544 (4)	C12—C17	1.394 (4)
C1—C9	1.535 (4)	C13—H13	0.9500
C2—H2	1.0000	C13—C14	1.395 (5)
C2—C3	1.500 (4)	C14—H14	0.9500
C2—N1	1.483 (4)	C14—C15	1.388 (5)
C3—C4	1.383 (5)	C15—H15	0.9500
C3—C8	1.400 (5)	C15—C16	1.390 (5)
C4—H4	0.9500	C16—H16	0.9500
C4—C5	1.383 (5)	C16—C17	1.389 (4)
C5—H5	0.9500	C17—C18	1.500 (4)
C5—C6	1.386 (5)	C18—H18a	0.9900
C6—H6	0.9500	C18—H18b	0.9900
C6—C7	1.393 (5)	O3—S1	1.463 (2)
C7—H7	0.9500	O4—S1	1.475 (2)
C7—C8	1.387 (5)	O5—S1	1.482 (2)
C8—C9	1.512 (5)	O6—S1	1.482 (2)
C1—O1—H1	109 (3)	N2—C11—C10	110.9 (3)
H1a—C1—O1	110.06 (15)	N2—C11—H11	110.21 (15)
C2—C1—O1	111.2 (2)	N2—C11—C12	112.4 (3)
C2—C1—H1a	110.06 (17)	C13—C12—C11	127.9 (3)
C9—C1—O1	112.5 (3)	C17—C12—C11	110.7 (3)
C9—C1—H1a	110.06 (17)	C17—C12—C13	121.4 (3)
C9—C1—C2	102.7 (2)	H13—C13—C12	120.72 (18)
H2—C2—C1	109.04 (16)	C14—C13—C12	118.6 (3)
C3—C2—C1	103.2 (2)	C14—C13—H13	120.7 (2)
C3—C2—H2	109.04 (15)	H14—C14—C13	119.8 (2)
N1—C2—C1	113.0 (2)	C15—C14—C13	120.5 (3)
N1—C2—H2	109.04 (16)	C15—C14—H14	119.8 (2)
N1—C2—C3	113.3 (3)	H15—C15—C14	119.7 (2)
C4—C3—C2	129.3 (3)	C16—C15—C14	120.5 (3)
C8—C3—C2	109.3 (3)	C16—C15—H15	119.75 (19)
C8—C3—C4	121.4 (3)	H16—C16—C15	120.33 (19)
H4—C4—C3	120.70 (19)	C17—C16—C15	119.3 (3)
C5—C4—C3	118.6 (3)	C17—C16—H16	120.33 (19)
C5—C4—H4	120.7 (2)	C16—C17—C12	119.7 (3)

H5—C5—C4	119.7 (2)	C18—C17—C12	110.9 (3)
C6—C5—C4	120.6 (3)	C18—C17—C16	129.4 (3)
C6—C5—H5	119.71 (19)	C17—C18—C10	103.0 (2)
H6—C6—C5	119.54 (19)	H18a—C18—C10	111.17 (19)
C7—C6—C5	120.9 (3)	H18a—C18—C17	111.17 (18)
C7—C6—H6	119.5 (2)	H18b—C18—C10	111.17 (17)
H7—C7—C6	120.5 (2)	H18b—C18—C17	111.17 (18)
C8—C7—C6	118.9 (3)	H18b—C18—H18a	109.1
C8—C7—H7	120.5 (2)	H1c—N1—H1b	103 (3)
C7—C8—C3	119.5 (3)	H1d—N1—H1b	107 (3)
C9—C8—C3	109.7 (3)	H1d—N1—H1c	107 (4)
C9—C8—C7	130.7 (3)	C2—N1—H1b	112 (2)
C8—C9—C1	102.8 (3)	C2—N1—H1c	118 (3)
H9a—C9—C1	111.21 (16)	C2—N1—H1d	108.6 (19)
H9a—C9—C8	111.21 (17)	H2b—N2—H2a	108 (3)
H9b—C9—C1	111.21 (17)	H2c—N2—H2a	109 (4)
H9b—C9—C8	111.21 (17)	H2c—N2—H2b	105 (4)
H9b—C9—H9a	109.1	C11—N2—H2a	117 (2)
C11—C10—H10	108.97 (17)	C11—N2—H2b	103 (2)
C18—C10—H10	108.97 (18)	C11—N2—H2c	114 (3)
C18—C10—C11	105.7 (2)	C10—O2—H2d	107 (3)
O2—C10—H10	108.97 (16)	O4—S1—O3	110.40 (14)
O2—C10—C11	113.3 (3)	O5—S1—O3	110.40 (13)
O2—C10—C18	110.8 (3)	O5—S1—O4	108.36 (14)
H11—C11—C10	110.21 (16)	O6—S1—O3	110.36 (13)
C12—C11—C10	102.7 (2)	O6—S1—O4	108.23 (13)
C12—C11—H11	110.21 (17)	O6—S1—O5	109.02 (13)

O1—C1—C2—C3	87.1 (3)	C6—C7—C8—C9	−176.3 (3)
O1—C1—C2—N1	−35.7 (3)	C10—C11—C12—C13	162.7 (2)
O1—C1—C9—C8	−86.7 (3)	C10—C11—C12—C17	−15.3 (3)
C1—C2—C3—C4	−156.1 (2)	C10—C18—C17—C12	16.7 (3)
C1—C2—C3—C8	21.6 (3)	C10—C18—C17—C16	−162.3 (2)
C1—C9—C8—C3	−21.1 (3)	C11—C12—C13—C14	−177.6 (3)
C1—C9—C8—C7	156.8 (2)	C11—C12—C17—C16	178.2 (3)
C2—C3—C4—C5	177.3 (3)	C11—C12—C17—C18	−0.9 (3)
C2—C3—C8—C7	−178.5 (2)	C12—C13—C14—C15	−0.2 (4)
C2—C3—C8—C9	−0.4 (3)	C12—C17—C16—C15	−0.3 (4)
C3—C4—C5—C6	0.1 (4)	C13—C14—C15—C16	0.0 (4)
C3—C8—C7—C6	1.3 (3)	C14—C15—C16—C17	0.3 (4)
C4—C5—C6—C7	0.6 (4)	C15—C16—C17—C18	178.6 (3)
C5—C6—C7—C8	−1.3 (4)		